

MATCHING LY_Α ABSORPTION TO NEARBY GALAXY HALOS WITH A LIKELIHOOD-BASED METHOD*

DAVID M. FRENCH, BART P. WAKKER

Department of Astronomy, University of Wisconsin - Madison

Draft version September 8, 2016

ABSTRACT

We present initial results from an ongoing large-scale study of the circumgalactic medium in the nearby Universe ($cz \leq 10,000$ km/s), using archival Cosmic Origins Spectrograph (COS) spectra of background QSOs. This initial sample contains 35 sight lines chosen for their proximity to large galaxies ($D \geq 25$ kpc) and high signal-to-noise ratio ($S/N \geq 11$), yielding 51 Ly_α systems which we have paired with nearby galaxies. We introduce a likelihood parameter to facilitate the matching of galaxies to absorption lines in a reproducible manner. We find the usual anti-correlation between Ly_α equivalent width (EW) and impact parameter (ρ) when we normalize by galaxy virial radius (R_{vir}). Galaxies associated with a Ly_α absorber are found to be more highly-inclined than the average distribution of galaxies in the survey volume at a $> 99\%$ confidence limit. Contrary to suggestions in other recent papers, we do not see obvious correlations with azimuth angle.

Subject headings: IGM, CGM, galaxies

1. INTRODUCTION

It is well known that galaxies must continue to accrete gas throughout their lifetimes in order to sustain their observed levels of star formation (e.g. Erb 2008, Putman et al. 2009b). This additional gas must come from the diffuse intergalactic medium (IGM), where the majority of the baryons in the universe reside (Penton et al. 2002, 2004; Lehner et al. 2007; Danforth & Shull 2008; Shull et al. 2012). How exactly this IGM gas eventually falls into the halos and disks of galaxies is still highly uncertain, as observational constraints are hard to come by. Because of the diffuse nature of IGM gas it is most readily and sensitively detected as absorption in the spectra of background active galactic nuclei (AGN). The advent of the sensitive UV spectrographs STIS and COS on the Hubble Space Telescope (HST) has provided a wealth of information on the properties and distribution of both the ions of heavy elements as well as the Lyman series of neutral H I gas around galaxies.

Individual concentrations of gas along a given sightline imprint absorption lines on the spectrum in the direction of the QSO. The metal lines trace the star formation history within the intervening gas, and neutral hydrogen lines (Ly_α) indicate both the location and velocities of outflowing gas, as well as the presence of fuel for future star formation. Numerous studies using these observations have shown that many Ly_α absorbers trace individual galaxy halos (e.g. Lanzetta et al 1995, Tripp et al. 1998, Chen et al. 1998, 2001a, Wakker & Savage 2009, Steidel et al. 2010, Prochaska et al. 2011, Thom et al 2012, Tumlinson et al. 2011 & 2013, Stocke et al. 2013 & 2014, Danforth et al. 2014, Liang et al 2014).

Some recent studies find that about half of Ly_α absorbers lie within galaxy haloes, at impact parameters

$\rho < 350$ kpc (Côté et al. 2005, Prochaska et al. 2006). In addition, Wakker & Savage (2009) find that an absorber lies within 400 kpc and 400 km/s for 90% of galaxies brighter than $0.1L_*$, and all galaxies have a Ly_α absorber within 1.5 Mpc. Higher redshift studies, such as Rudie et al. (2012) at $2 < z < 3$, find evidence for an elevated density of absorbers up to 2 Mpc from galaxies. Wakker & Savage (2009) also discovered a correlation between Ly_α absorption linewidth and impact parameter ρ , observing that the broadest lines ($FWHM > 150$ km/s) are only seen within 350 kpc of a galaxy, while at $\rho > 1$ Mpc, only lines with $FWHM < 75$ km/s occur. This suggests that the temperature and/or turbulence of gas increases in the presence of galaxies.

In addition, studying the enrichment of galaxy halos is necessary for constraining outflow models and informing stellar feedback prescriptions. Directly measuring the velocity field and column densities of absorbers as a function of impact parameter and orientation around galaxies would provide the clearest evidence of inflow or outflow activity, but results are still uncertain. Kacprzak et al. (2011) claim to find that Mg II equivalent widths correlate with galaxy inclination, but Mathes et al. (2014) find no such correlation for Ly_α and O VI absorbers. Furthermore, we should expect outflowing gas to be more highly enriched and trace the metallicity of the associated galaxy, with inflowing gas instead appearing only in H I. Both Stocke et al. (2013) and Liang & Chen (2014) find an “edge” to heavy ion absorption at $\sim 0.5R_{vir}$, but with Ly_α covering fractions of $\sim 0.75 - 1$ continuing out to R_{vir} . However, Mathes et al. (2014) measures O VI absorption out to $\sim 3R_{vir}$, and Savage et al. (2014) find that more than half of O VI absorption occurs beyond 1 R_{vir} .

Recent results from Kacprzak et al. (2011 & 2012) suggest that absorbing systems have a preferred orientation with respect to the major and minor axes of the galaxies they are associated with. This could be evidence of inflows and outflows, or an effect of the global structure of galaxy halos, but the statistics are not yet good enough to provide consistent answers. A larger-scale study of in-

* This research has made use of the NASA/IPAC Extragalactic Database (NED) which is operated by the Jet Propulsion Laboratory, California Institute of Technology, under contract with the National Aeronautics and Space Administration. Based on observations with the NASA/ESA *Hubble Space Telescope*, obtained at the Space Telescope Institute, which is operated by AURA, Inc., under NASA contract NAS 5-26555.

clination and azimuthal angles vs. absorber properties is needed in order to elucidate the distribution of absorbing systems around galaxies. This is most easily done for the largest galaxies in the nearby universe, where it is possible to obtain inclinations and unambiguous absorber associations.

Previous studies have suffered from small sample sizes (e.g. Mathes et al. 2014 use 14 galaxies, Stocke et al. 2013 use 11, Werk et al. 2014 use 44), and incompleteness due to their higher mean redshifts (e.g. the Mathes et al. 2014 sample is $0.12 < z < 0.67$, and Werk et al. 2014 are complete to $\sim L^*$ at $z \sim 0.2$). To address these shortcomings, we are conducting a large survey of the properties of intergalactic gas in the nearby universe, where we have good and relatively complete information on both faint and bright galaxies, in order to reveal how the IGM and galaxies affect each other. We are taking advantage of the over 500 archived QSO and Seyfert spectra taken by the Cosmic Origins Spectrograph (COS) and Space Telescope Imaging Spectrograph (STIS) on the Hubble Space Telescope (HST), combined with the wealth of information available for the $\sim 100,000$ galaxies with $cz < 10,000$ km/s found in the NASA Extragalactic Database (NED) to probe the environment of absorbing gas systems in the nearby universe. This approach allows for an unbiased understanding of the distribution of the gas around galaxies, which requires looking for both detections and non-detections of gas, both near as well as far away from galaxies.

This paper presents initial results from our pilot study of 35 sight lines, chosen for their proximity to large galaxies and high signal-to-noise spectra. This paper is organized as follows: in Section 2 we present the data and analysis techniques, in Section 3 we present the results, and in Section 4 we discuss possible interpretations of our results.

2. DATA AND ANALYSIS

2.1. Galaxy Data

The goal of this study relies on knowing the locations and properties of all galaxies near detected Ly α absorption lines. To facilitate this, we have constructed a dataset of all $z \leq 0.033$ ($cz \leq 10,000$ km/s) galaxies with published data available through the NASA Extragalactic Database (NED). A full description of this catalog will be presented in French & Wakker 2017 (in prep.). Here we summarize its important aspects.

The galaxy dataset contains over 108,000 entries, and includes data from SDSS, 2MASS, 2dF, 6dF, RC3, and many other, smaller surveys. Our criteria for including a galaxy in this dataset is only an accurate, spectroscopic redshift which places the galaxy in the $cz \leq 10,000$ km/s velocity range. This restriction leads to a completeness limit of $B \lesssim 18.7$ mag, or $\sim 0.2L_*$, at $cz = 10,000$ km/s, and progressively better towards lower velocities (see Figure 1). This limit will vary depending on which major surveys include a particular region of the sky. The major contributor is whether or not SDSS data is available, which begins around $cz = 5,000$ km/s. Figure 1 is split into 4 velocity bins to illustrate this. Our data is complete down to $\sim 0.1L_*$ in the first bin, $0 \leq cz \leq 2,500$ km/s. At slightly higher velocity, $2500 \leq cz \leq 6000$ km/s, the completeness falls to barely better than $\sim 1.0L_*$ as

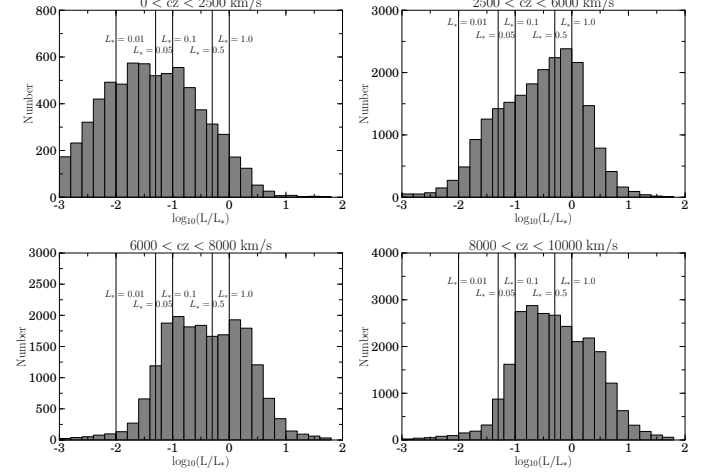


Figure 1. Distribution of L/L_* values for all galaxies in the dataset. Black vertical lines highlight 1, 0.5, 0.1, 0.05 and 0.01 L_* . The turnover around $0.1L_*$ shows that on average, the dataset is complete to $0.1L_*$.

we move past the near and well studied galaxies, but have yet to reach the footprint of deep all sky surveys. SDSS data becomes available in the last two bins, spanning $6000 \leq cz \leq 10,000$ km/s, and correspondingly completeness remains high down to the SDSS limits of $B \lesssim 18.7$ mag, or $\sim 0.2L_*$ at $cz = 10,000$ km/s.

Additionally, we have homogenized the galaxy data beyond the steps taken by NED by normalizing all measurements of galaxy inclination, position angle, and diameter to 2MASS K -band values. Most galaxies in NED have measures of inclination, position angle and diameter available in several different bands, so in order to make meaningful comparisons it is necessary to automatically choose one band for all measurements. We chose 2MASS values for this because it was an all-sky survey, and represents the largest fraction of available galaxy data. Physical galaxy diameters are derived from 2MASS K_s “total” angular diameter measurements and galaxy distances. 2MASS K_s “total” diameter estimates are surface brightness extrapolation measurements and are derived as

$$r_{tot} = r' + a(\ln(148))^b, \quad (1)$$

where r_{tot} is defined as the point where the surface brightness extends to 5 disk scale lengths, r' is the starting point radius ($> 5'' - 10''$ beyond the nucleus, or core influence), and a and b are Sersic exponential function scale length parameters ($f = f_0 \exp(-r/a)^{(1/b)}$, see Jarrett et al. 2003 for a full description). Approximately 50% of all the galaxies have this 2MASS K_s “total” diameter. Of the remainder, 20% have SDSS diameters, 27% have no published diameter, and 3% have diameters from other surveys. We convert values in these other bands to 2MASS K_s “total” diameters via a simple least squares linear fit when necessary.

We used B -band magnitudes to estimate each galaxy’s luminosity in units of L_* as follows:

$$\frac{L}{L_*} = 10^{-0.4(M_B - M_{B*})}. \quad (2)$$

Target	R.A.	Dec.	z	Program	Grating	Obs ID	Obs Date	T_{exp} [ks]	S/N [1238]
1H0717+714	7.0 21.0 53.3	71.0 20.0 36.0	0.5003	12025	G130M	Obs ID	Obs Date	6000	37
1H0717+714	7.0 21.0 53.3	71.0 20.0 36.0	0.5003	12025	G160M	Obs ID	Obs Date	8252	31
2dFGRS_S393Z082	2.0 45.0 0.8	-30.0 7.0 23.0	0.3392	12988	G130M	Obs ID	Obs Date	17668	10
3C66A	2.0 22.0 39.6	43.0 2.0 8.0	0.4440	12612	G130M	Obs ID	Obs Date	12600	24
3C66A	2.0 22.0 39.6	43.0 2.0 8.0	0.4440	12863	G160M	Obs ID	Obs Date	7227	15
3C66A	2.0 22.0 39.6	43.0 2.0 8.0	0.4440	1371	G160M	Obs ID	Obs Date	2106	1
FBQ SJ1431+2442	14.0 31.0 25.8	24.0 42.0 20.0	0.4069	12603	G130M	Obs ID	Obs Date	16501	17
H1101-232	11.0 3.0 37.7	-23.0 29.0 31.0	0.1860	12025	G130M	Obs ID	Obs Date	13341	16
H1101-232	11.0 3.0 37.7	-23.0 29.0 31.0	0.1860	12025	G160M	Obs ID	Obs Date	13296	10
HE0241-3043	2.0 43.0 37.7	-30.0 30.0 48.0	0.6693	12988	G130M	Obs ID	Obs Date	6972	14
LBQS1230-0015	12.0 33.0 4.1	-0.0 31.0 34.0	0.4709	11598	G130M	Obs ID	Obs Date	10323	13
LBQS1230-0015	12.0 33.0 4.1	-0.0 31.0 34.0	0.4709	11598	G160M	Obs ID	Obs Date	5896	7
MRC2251-178	22.0 54.0 5.9	-17.0 34.0 55.0	0.0661	12029	G130M	Obs ID	Obs Date	5515	42
MRC2251-178	22.0 54.0 5.9	-17.0 34.0 55.0	0.0661	12029	G160M	Obs ID	Obs Date	7125	30
MRK290	15.0 35.0 52.3	57.0 54.0 9.0	0.0296	11524	G130M	Obs ID	Obs Date	3856	38
MRK290	15.0 35.0 52.3	57.0 54.0 9.0	0.0296	11524	G160M	Obs ID	Obs Date	4800	18
MRK290	15.0 35.0 52.3	57.0 54.0 9.0	0.0296	6590	G160M	Obs ID	Obs Date	7152	12
MRK876	16.0 13.0 57.2	65.0 43.0 10.0	0.1290	11524	G130M	Obs ID	Obs Date	12579	65
MRK876	16.0 13.0 57.2	65.0 43.0 10.0	0.1290	11686	G160M	Obs ID	Obs Date	11819	44
MRK1014	1.0 59.0 50.2	0.0 23.0 41.0	0.1630	12569	G130M	Obs ID	Obs Date	1828	17
PG0832+251	8.0 35.0 35.9	24.0 59.0 41.0	0.3310	12025	G130M	Obs ID	Obs Date	6134	14
PG0832+251	8.0 35.0 35.9	24.0 59.0 41.0	0.3310	12025	G160M	Obs ID	Obs Date	6757	9
PG0003+158	0.0 5.0 59.3	16.0 9.0 49.0	0.4509	12038	G130M	Obs ID	Obs Date	10361	25
PG0003+158	0.0 5.0 59.3	16.0 9.0 49.0	0.4509	12038	G160M	Obs ID	Obs Date	10851	20
PG1001+054	10.0 4.0 20.1	5.0 13.0 1.0	0.1610	13347	G130M	Obs ID	Obs Date	5233	14
PG1001+054	10.0 4.0 20.1	5.0 13.0 1.0	0.1610	13347	G160M	Obs ID	Obs Date	3838	10
PG1302-102	13.0 5.0 33.0	-10.0 33.0 20.0	0.2784	12038	G130M	Obs ID	Obs Date	5979	27
PG1302-102	13.0 5.0 33.0	-10.0 33.0 20.0	0.2784	12038	G160M	Obs ID	Obs Date	6867	34
RBS1768	21.0 38.0 49.7	-38.0 28.0 40.0	0.1830	12936	G130M	Obs ID	Obs Date	6962	24
RBS1768	21.0 38.0 49.7	-38.0 28.0 40.0	0.1830	12936	G160M	Obs ID	Obs Date	3837	11
RX_J0714.5+7408	7.0 14.0 36.2	74.0 8.0 11.0	0.3710	12275	G130M	Obs ID	Obs Date	8333	18
RX_J1017.5+4702	10.0 17.0 30.9	47.0 2.0 25.0	0.3354	13314	G130M	Obs ID	Obs Date	8655	12
RX_J1117.6+5301	11.0 17.0 40.5	53.0 1.0 50.0	0.1587	14240	G130M	Obs ID	Obs Date	4943	11
RX_J1236.0+2641	12.0 36.0 4.1	26.0 41.0 36.0	0.2092	12248	G130M	Obs ID	Obs Date	4235	11
RX_J1236.0+2641	12.0 36.0 4.1	26.0 41.0 36.0	0.2092	12248	G160M	Obs ID	Obs Date	6800	6
RX_J1330.8+3119	13.0 30.0 53.2	31.0 19.0 32.0	0.2423	12248	G130M	Obs ID	Obs Date	4262	11
RX_J1330.8+3119	13.0 30.0 53.2	31.0 19.0 32.0	0.2423	12248	G160M	Obs ID	Obs Date	6845	11
RX_J1356.4+2515	13.0 56.0 25.6	25.0 15.0 23.0	0.1640	12248	G130M	Obs ID	Obs Date	2282	10
RX_J1356.4+2515	13.0 56.0 25.6	25.0 15.0 23.0	0.1640	12248	G160M	Obs ID	Obs Date	2793	6
RX_J1503.2+6810	15.0 3.0 16.5	68.0 10.0 6.0	0.1140	12276	G130M	Obs ID	Obs Date	1932	11
RX_J1544.5+2827	15.0 44.0 30.5	28.0 27.0 56.0	0.2314	13423	G130M	Obs ID	Obs Date	2096	10
RX_J2043.1+0324	20.0 43.0 6.2	3.0 24.0 50.0	0.2710	13840	G130M	Obs ID	Obs Date	7834	15
RX_J2139.7+0246	21.0 39.0 44.2	2.0 46.0 5.0	0.2600	13840	G130M	Obs ID	Obs Date	7854	16
SBS0957+599	10.0 1.0 2.6	59.0 44.0 15.0	0.7475	12248	G130M	Obs ID	Obs Date	3300	12
SBS0957+599	10.0 1.0 2.6	59.0 44.0 15.0	0.7475	12248	G160M	Obs ID	Obs Date	5201	11
SDSS J021218.32-073719.8	2.0 12.0 18.3	-7.0 37.0 20.0	0.1739	12248	G130M	Obs ID	Obs Date	6525	12
SDSS J021218.32-073719.8	2.0 12.0 18.3	-7.0 37.0 20.0	0.1739	12248	G160M	Obs ID	Obs Date	6780	7
SDSS J080838.80+051440.0	8.0 8.0 38.8	5.0 14.0 40.0	0.3606	12603	G130M	Obs ID	Obs Date	4674	8
SDSS J091728.60+271951.0	9.0 17.0 28.6	27.0 19.0 51.0	0.0756	14071	G130M	Obs ID	Obs Date	15471	10
SDSS J112224.10+031802.0	11.0 22.0 24.1	3.0 18.0 2.0	0.4753	12603	G130M	Obs ID	Obs Date	7588	10
SDSS J130524.30+035731.0	13.0 5.0 24.3	3.0 57.0 31.0	0.5457	12603	G130M	Obs ID	Obs Date	7588	13
SDSS J135726.27+043541.4	13.0 57.0 26.2	4.0 35.0 41.0	1.2345	12264	G130M	Obs ID	Obs Date	14148	15
SDSS J135726.27+043541.4	13.0 57.0 26.2	4.0 35.0 41.0	1.2345	12264	G160M	Obs ID	Obs Date	28206	12
SDSS J140428.30+335342.0	14.0 4.0 28.3	33.0 53.0 42.0	0.5500	12603	G130M	Obs ID	Obs Date	7705	7
TON1009	9.0 9.0 6.1	32.0 36.0 31.0	0.8103	12603	G130M	Obs ID	Obs Date	4740	11

Table 1

COS targets in this sample. Each line corresponds to a single grating observation, so some individual S/N ratios listed may be below the required minimum of 11 for the final, combined spectra.

We adopt the CfA galaxy luminosity function by Marzke et al. (1994), which sets $B_* = -19.57$. Direct B band measurements are available for $\sim 30\%$ of galaxies, and most of the rest have SDSS g and r magnitudes, which can be converted to B via $B = g + 0.39(g-r) + 0.21$ (Jester et al. 2005). Finally, we also compute an estimate of the virial radius of each galaxy as $\log R_{vir} = 0.69 \log D + 1.24$. This follows the parametrization of Stocke et al. (2013) relating a galaxy's luminosity to its virial radius, and the Wakker & Savage (2009) empirical relation between diameter and luminosity (see Wakker et al. 2015 and references therein for further details). Errors are propagated from the original published magnitude errors.

This homogeneous galaxy data table allows us to draw direct comparisons between the properties of the absorbers and the properties, separations, and environments of nearby galaxies with unprecedented completeness. The full dataset will be publicly released and discussed in further detail in a forthcoming paper (French et al. 2017, in prep).

2.2. Spectra

This initial pilot study contains 35 sightlines to bright QSOs observed with COS. We chose sightlines by first sorting the galaxy data table described above by galaxy diameter. This sorted list is then correlated with the full list of publicly available sightlines, and only those systems with impact parameter less than 500 Mpc and galaxy diameter, D , greater than 25 kpc are kept. Finally, we select the top 35 sightlines with $S/N > 11$, as sorted by galaxy diameter.

All COS spectra for the target sightlines were obtained through the Barbara A. Mikulski Archive for Space Telescopes (MAST), and processed with CALCOS v3.0 or later. We combined individual exposures by the method of Wakker et al. (2015), which corrects the COS wavelength scale by cross-correlating all ISM and IGM lines in each exposure. This method addresses the up to ± 40 km/s misalignments produced by CALCOS, and produces a corrected error array based on Poisson noise, which better matches the measured errors than the errors delivered in the x1d files. We then combine multiple exposures by aligning Galactic absorption lines with 21-cm spectra, and adding up the total counts in each pixel before converting to flux using the original, average flux-count ratio at each wavelength.

3. RESULTS

We have identified 51 Ly α absorption lines in the spectra of our initial 35 QSO sample which can be unambiguously associated with a single nearby galaxy of diameter $D \geq 25$ kpc. In order to be considered for a pairing, a galaxy and absorption feature must appear within 400 km/s in velocity and 500 kpc in physical impact parameter from each other. When multiple galaxies pass these criteria for a particular line, we are left with two options. 1) one galaxy is obviously far larger and closer in physical and velocity space to the line, and may have several satellite galaxies, or 2) no single galaxy if obviously dominant, and we do not include this line in further analysis.

To facilitate this decision, we calculate the likelihood, \mathcal{L} , of every possible galaxy-absorber pairing as follows:

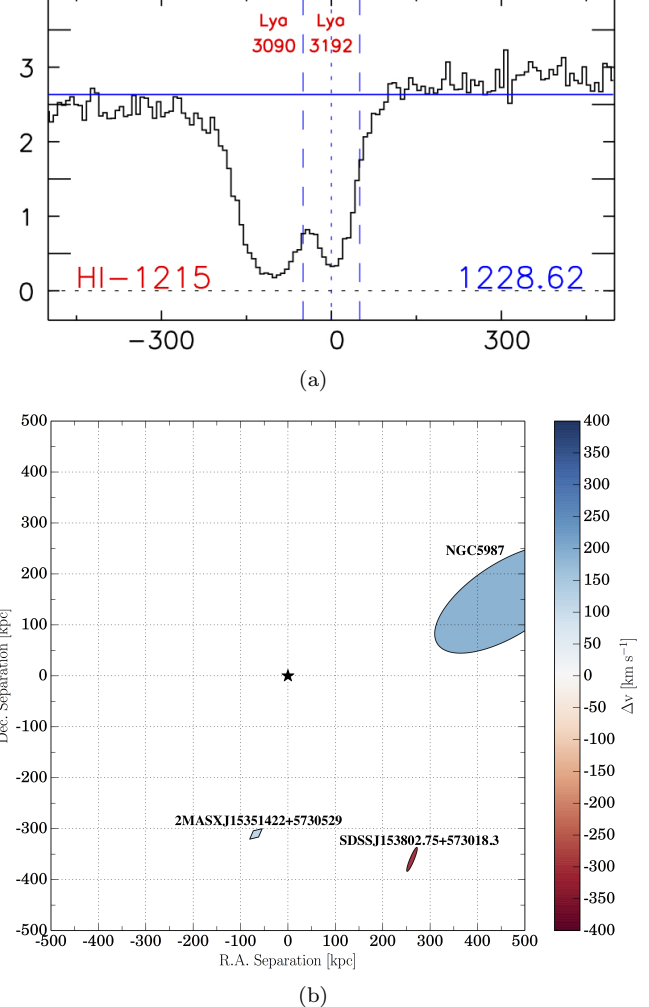


Figure 2. a) An example of Ly α lines found in a sightline towards target MRK290 at 3090 and 3192 km/s. b) A map of all galaxies within a 500 kpc impact parameter of target MRK290 sightline and with velocity (cz) within 400 km/s of absorption detected at 3090 and 3192 km/s (central black star). The galaxy NGC5987 ($v = 3010$ km/s, inclination = 65°) can be unambiguously paired with the Ly α absorption features at $v = 3090, 3192$ km/s because it is the largest and closest galaxy in both physical and velocity space to the absorption feature.

$$\mathcal{L} = Ae^{-(\frac{\rho}{R_{eff}})^2} e^{-(\frac{\Delta v}{200})^2}. \quad (3)$$

Here ρ is the physical impact parameter, Δv the velocity difference between the absorber and the galaxy ($\Delta v = v_{galaxy} - v_{absorber}$), and A is a factor included to increase the likelihood in the case that $R_{eff} \geq \rho$ (in which case $A = 2$, otherwise $A = 1$). We compute \mathcal{L} for two different values of R_{eff} : R_{vir} , the virial radius of the galaxy, and $d^{1.5}$, the major diameter of the galaxy to the power of 1.5. \mathcal{L} computed with R_{vir} is liable to select satellite galaxies instead of the larger hosts, so including a version with $d^{1.5}$ serves as a two-tiered selection system. An absorber-galaxy system separated by 200 km/s in velocity and $1R_{vir}$ would have $\mathcal{L} = 0.27$. In order for an absorber to be marked as “associated” with a particular galaxy, we

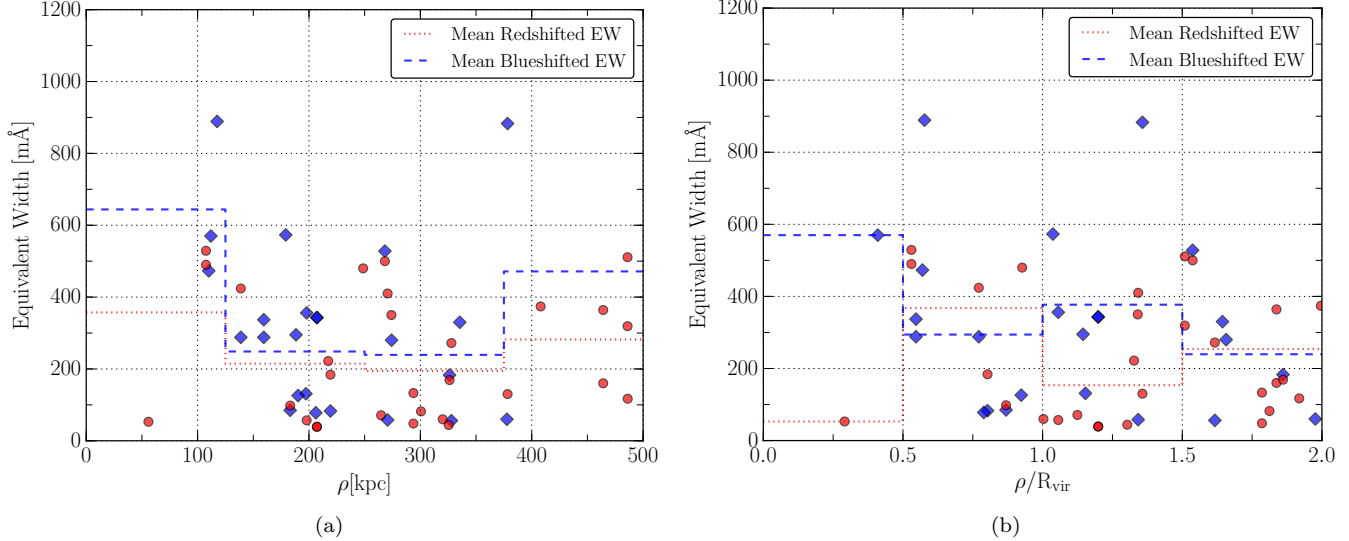


Figure 3. a) Equivalent width of each absorber as a function of impact parameter, ρ (kpc), b) Equivalent width as a function of ρ/R_{vir} . The anti-correlation is strongest when scaling ρ by the galaxy virial radius. Absorbers are separated into red and blue-shifted samples based on Δv . Bins of mean EW are overplotted in red-dashed, and blue-dotted lines for their respective samples.

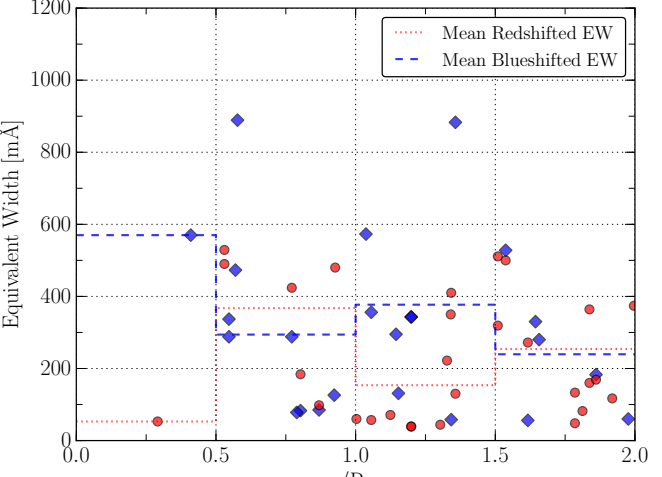
require that its \mathcal{L} must be a factor of 5 larger than the next best possible association, and $\mathcal{L} \geq 0.01$ for at least one of $\mathcal{L}_{R_{\text{vir}}}$ or $\mathcal{L}_{D^{1.5}}$. We visually inspect systems with only one \mathcal{L} meeting these criteria, and decide to reject or include it based on the complexity of the nearby galaxy environment.

Figures 2.2 and 2(b) show a clean example of a Ly α absorption line with a map of its galaxy environment, showing an unambiguous pairing between the absorption features at 3090, 3192 km/s toward MRK290 and galaxy NGC5987 ($\mathcal{L} = 0.37$). Unless explicitly stated, all following analysis concerns similarly unambiguous “associated” systems.

Additionally, we split the absorber-galaxy catalog based on the velocity difference of the two, Δv . With this scheme, we refer to an absorber with a velocity *lower* than the associated galaxy as *blueshifted*, while an absorber with a velocity *higher* is referred to as *redshifted*. The rest of the results will be analyzed based upon this splitting.

3.1. EW - ρ Anti-correlation

Numerous previous studies have suggested that Ly α equivalent width (EW) is anti-correlated with impact parameter (ρ) to the nearest galaxy. We find a weak correlation, as shown in Figure 3(a). However, we find a stronger anti-correlation when we normalize ρ by R_{vir} . Figure 3(b) shows this expected anti-correlation when plotting EW vs ρ/R_{vir} . A possible explanation for this trend is that larger galaxies host larger, more physically extended CGM halos. We would thus expect the absorber EW to also correlate positively with R_{vir} . Figure 4(a) shows EW as a function of R_{vir} , with the blue-dashed and red-dotted lines show the average EW in bins of 50 kpc of R_{vir} , showing little evidence of a correlation. However, by similarly plotting ρ as a function of R_{vir} , we instead find some evidence that absorbers around larger galaxies tend to be found at higher impact parameters.



While we expect the upper-left quadrant of this figure to be sparsely populated (our likelihood-based method would tend not to choose small galaxies at large distances), it is unclear to us why the lower-right quadrant (large galaxies with absorbers at low impact parameter) is also sparsely populated. The full-sized sample at the completion of our study should provide a clearer picture of this intriguing result **MORE?**.

3.2. Inclination

In this section we examine the inclinations of the associated galaxies compared to the distributions of absorbers. We correct for the finite thickness of galaxies, which causes b/a to deviate from $\cos i$ at high inclinations, by computing galaxy inclinations with the following formula from Heidmann et al. (1972a):

$$\cos(i) = \sqrt{\frac{q^2 - q_0^2}{1 - q_0^2}}, \quad (4)$$

where $q = b/a$, the ratio of the minor to major axis, and q_0 is the intrinsic axis ratio, set to $q_0 = 0.2$ for all galaxies (e.g., Jones, Davies, and Trewella 1996).

Figure 5 shows red and blueshifted absorbers’ EW plotted against the inclinations of their associated galaxies. We note that there is a clear excess of absorbers near galaxies of high inclination, with 75% of redshifted and 65% of blueshifted absorbers being associated with galaxies of $i \geq 50$ deg. The solid-black and dashed-grey lines show mean and 90th percentile histograms, respectively, in bins of 12 deg. There does not appear to be much evolution of EW across galaxy inclination, although a slight increase of mean EW is possibly present towards higher inclinations. There are only 3 absorbers associated with a galaxy with $i < 35$

In total 65% of blueshifted and 75% of redshifted absorbers are associated with high inclined galaxies ($i \geq 50$ deg). Only 56% of all galaxies in the survey volume

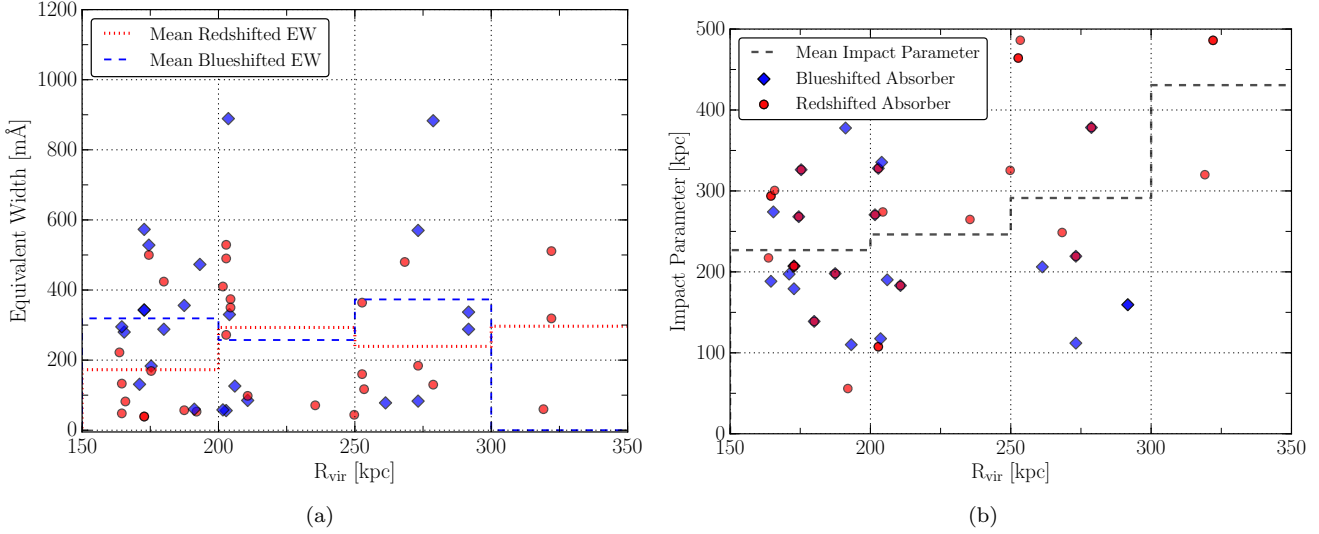


Figure 4. a) Equivalent width of each absorber as a function of the virial radius of the associated galaxy. The blue-dotted and red-dashed lines shows the average EW in 50 kpc bins of impact parameter for the blueshifted and redshifted absorbers, respectively. b) Impact parameter to each absorber as a function of the virial radius of the associated galaxy. The blue-dotted and red-dashed lines shows the average impact parameter in 50 kpc bins of R_{vir} for the blueshifted and redshifted absorbers, respectively.

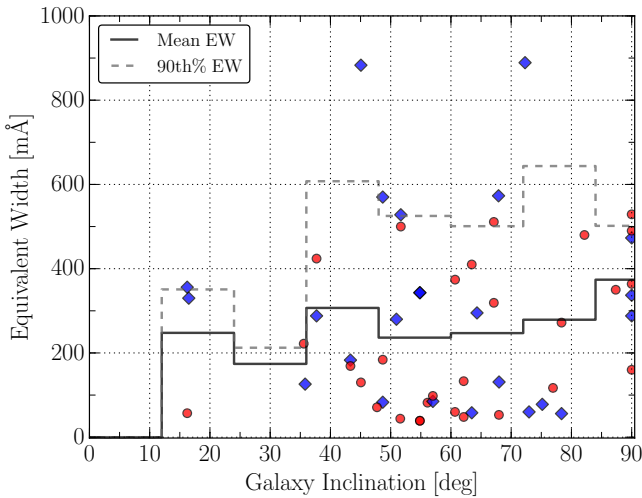


Figure 5. Equivalent width of each absorber as a function of the inclination angle of the associated galaxy. The dashed black line shows the mean EW of all absorbers in bins of 15°.

are highly inclined, indicating a preference for detecting absorption around inclined galaxies. Figure 6 shows the distribution of galaxy inclinations for both the red and blue-shifted associated galaxies and all galaxies within the survey volume. We tested the difference between the full distribution of inclination angles and the distribution for all (red + blue-shifted) associated galaxies using the Anderson-Darling (AD) and Kolmogorov-Smirnov (KS) statistical distribution tests, yielding p-values of $KS_p = 0.0368$, and $AD_p = 0.00014$. Hence, there appears to be a significant bias towards detecting Ly α absorption around highly inclined galaxies.

It is worth noting here that the observed distribution of galaxy inclinations is *not* flat, as one might expect. Because our galaxy sample is essentially magnitude-limited, highly-inclined and optically thin galaxies can

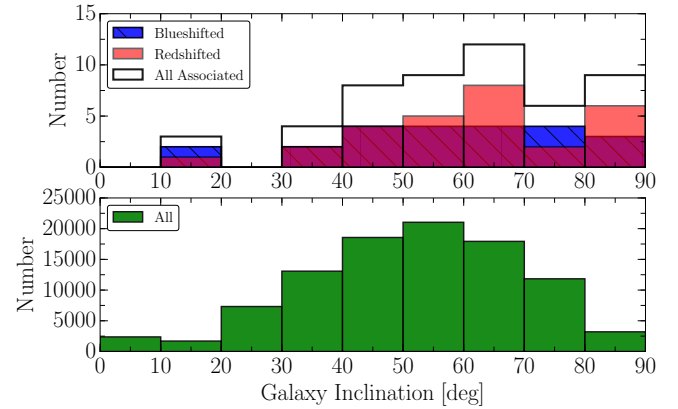


Figure 6. **Top:** Distribution of inclinations for all associated galaxies, split into red and blue shifted sets. **Bottom:** Distribution of inclination of all galaxies in the $cz \leq 10,000$ km/s redshift range.

be detected out to larger distances and are thus over-represented in the sample (Jones, Davies and Trewella 1996). It is possible that this effect is also responsible for the over-abundance of Ly α detections around highly inclined galaxies. If we assume a disk or oblate spheroid shape and some covering fraction for the CGM, the probability of encountering a cloud near an inclined galaxy would increase with the increased path-length through the halo.

3.3. Velocity Difference (Δv)

We find evidence for an anti-correlation between absorber EW and the velocity difference between the galaxy and the associated absorption, Δv . The mean and maximal EW of absorption increases with decreasing Δv (see Figure 7). In total, 35/51 (69%) of absorbers are found within ± 100 km/s. This ± 100 km/s threshold also applies to absorber EW , with only 1 absorber of $EW \geq 400$ found with $\Delta v > 100$ km/s. Blueshifted ab-

Target	Galaxy	\mathcal{L}	R_{vir} [kpc]	ρ (kpc) [kpc]	v_{galaxy} [km/s]	Δv [km/s]	Inc. [deg]	Az. [deg]	$v_{Ly\alpha}$ [km/s]	$W_{Ly\alpha}$ [mÅ]
(1)	(2)	(3)	(4)	(5)	(6)	(7)	(8)	(9)	(10)	(11)
1H0717+714	UGC03804	0.24	173	207	2887	17	53	7	2870	343±6
1H0717+714	UGC03804	0.21	173	207	2887	-69	53	7	2956	39±4
2dFGRS_S393Z082	NGC1097	1.8*	273	112	1271	32	47	12	1239	570±21
3C66A	UGC01832	1.7	192	56	5913	-52	65	16	5965	53±6
FBQSJ1431+2442	IRASF14291+2443	0.074*	203	328	6615	73	74	x	6542	56±15
FBQSJ1431+2442	IRASF14291+2443	0.085*	203	328	6615	-8	74	x	6623	272±20
H1101-232	MCG-04-26-019	0.33	173	179	3623	43	65	26	3580	573±12
HE0241-3043	NGC1097	1.4*	273	219	1271	50	47	62	1221	83±12
HE0241-3043	NGC1097	1.4*	273	219	1271	-39	47	62	1310	184±15
LBQS1230-0015	NGC4517	1.4	193	110	1128	1	83	90	1127	473±16
MRC2251-178	MCG-03-58-009	1.4*	319	320	9030	-21	59	39	9051	60±4
MRK1014	NGC0768	0.12*	253	486	7021	-59	73	85	7080	117±11
MRK290	NGC5987	0.77*	322	486	3010	-95	65	12	3105	511±5
MRK290	NGC5987	0.37*	322	486	3010	-197	65	12	3207	319±4
MRK876	UGC10294	0.063	165	274	3504	26	50	7	3478	280±3
PG0003+158	NGC7814	0.081	171	197	1050	217	65	47	833	131±15
PG0832+251	KUG0833+252	0.041	165	294	6964	-16	60	55	6980	133±14
PG0832+251	KUG0833+252	0.01	165	294	6964	-237	60	55	7201	48±10
PG1001+054	UGC05432	0.14	164	217	3995	-97	35	78	4092	222±10
PG1302-102	NGC4939	0.05*	235	265	3110	-338	46	61	3448	71±5
RBS1768	RFGC3781	0.056*	253	464	9162	-198	81	x	9360	364±4
RBS1768	RFGC3781	0.024*	253	464	9162	-272	81	x	9434	160±5
RX_J0714.5+7408	UGC03717	0.13*	202	271	4188	114	61	83	4074	58±7
RX_J0714.5+7408	UGC03717	0.15*	202	271	4188	-76	61	83	4264	410±9
RX_J1017.5+4702	NGC3198	0.02	191	378	663	34	70	55	629	60±17
RX_J1117.6+5301	NGC3631	0.32	187	198	1156	25	16	x	1131	356±20
RX_J1117.6+5301	NGC3631	0.25	187	198	1156	-103	16	x	1259	57±17
RX_J1236.0+2641	NGC4565	0.54*	292	159	1230	218	83	39	1012	337±32
RX_J1236.0+2641	NGC4565	1.7*	292	159	1230	42	83	39	1188	288±24
RX_J1236.0+2641	NGC4559	0.27	165	188	807	12	62	31	795	295±37
RX_J1330.8+3119	UGC08492	0.081*	204	335	7414	13	16	41	7401	330±15
RX_J1356.4+2515	CGCG132-055	0.35*	206	190	8671	196	35	25	8475	126±18
RX_J1503.2+6810	CGCG318-012	0.031*	250	325	9765	-357	50	1	10122	44±14
RX_J1544.5+2827	CGCG166-047	0.031	175	326	9646	4	42	61	9642	183±14
RX_J1544.5+2827	CGCG166-047	0.023	175	326	9646	-113	42	61	9759	169±12
RX_J2043.1+0324	NGC6954	0.037	166	301	4067	-13	55	66	4080	82±10
RX_J2139.7+0246	UGC11785	1.5	203	108	4074	-9	80	69	4083	490±7
RX_J2139.7+0246	UGC11785	1.2*	203	108	4074	-107	80	69	4181	529±7
SBS0957+599	MCG+10-14-058	1.4*	261	206	9501	32	71	19	9469	78±12
SDSSJ021218.32-073719.8	SDSSJ021315.79-073942.7	0.09	174	268	4800	44	50	10	4756	528±15
SDSSJ021218.32-073719.8	SDSSJ021315.79-073942.7	0.092	174	268	4800	-33	50	10	4833	500±17
SDSSJ080838.80+051440.0	UGC04239	0.87*	279	378	8763	23	44	38	8740	883±24
SDSSJ080838.80+051440.0	UGC04239	0.45*	279	378	8763	-164	44	38	8927	130±19
SDSSJ091728.60+271951.0	UGC04895	0.022*	204	408	7073	-68	59	32	7141	374±23
SDSSJ112224.10+031802.0	NGC3640	0.4	180	139	1251	202	37	22	1049	288±30
SDSSJ112224.10+031802.0	NGC3640	1.1	180	139	1251	-13	37	22	1264	424±27
SDSSJ130524.30+035731.0	UGC08186	1.3*	268	249	7006	-33	76	14	7039	480±14
SDSSJ135726.27+043541.4	NGC5364	0.74*	211	183	1241	117	55	84	1124	85±11
SDSSJ135726.27+043541.4	NGC5364	0.97*	211	183	1241	-55	55	84	1296	98±9
SDSSJ140428.30+335342.0	KUG1402+341	1.4	204	118	7919	35	69	63	7884	889±28
TON1009	NGC2770	0.19*	204	274	1947	-14	78	43	1961	350±21

Table 2

All associated systems. The largest \mathcal{L} value is given, where a (*) indicates $d^{1.5}$ was used, otherwise the quoted \mathcal{L} was computed with R_{vir} . For all entries, 'x' indicates unknown values.

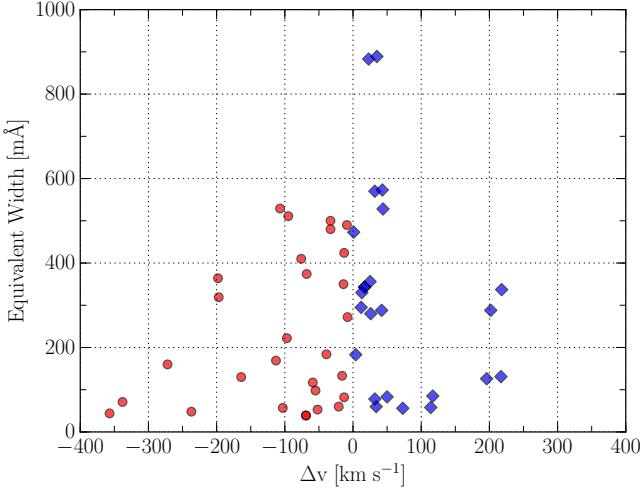


Figure 7. Equivalent width as a function of the velocity separation between the galaxy and absorption line.

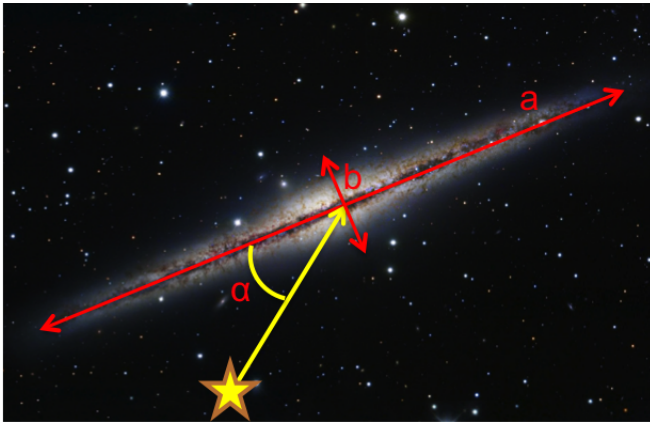


Figure 8. Azimuth is the angle, α , between the major axis of the galaxy, a , and a vector extending from the AGN target to the galaxy center. Image of NGC891 credit: Composite Image Data - Subaru Telescope (NAOJ), Hubble Legacy Archive, Michael Joner, David Laney (West Mountain Observatory, BYU); Processing - Robert Gendler.

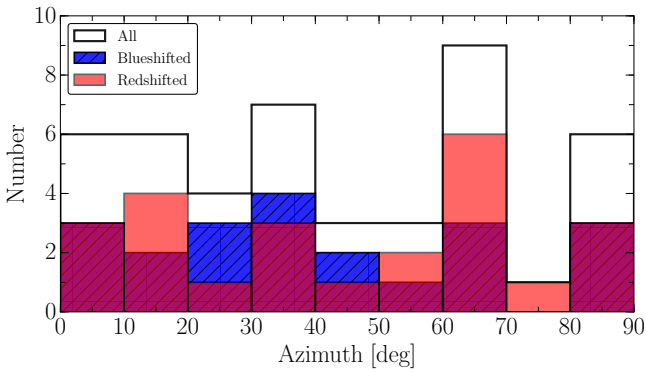


Figure 9. The distributions of azimuth angles for red and blue-shifted samples, with the combined sample plotted in black. $Azimuth = 0$ corresponds to along the projected major axis of the galaxy, and $azimuth = 90$ is along the minor axis.

sorbers are on average closer to their associated galaxy, with $\overline{\Delta v}_{blue} = 68$, compared to $\overline{\Delta v}_{red} = -102$ for the redshifted sample, and correspondingly have higher average equivalent width, $\overline{EW}_{blue} = 317 \pm 18$ compared to $\overline{EW}_{red} = 329 \pm 12$.

Additionally, of the 51 associated absorbers, 31 are matched with the same galaxy as another absorber (for a total of 15 unique galaxies in this subset). All but one of these cases involve two absorbers in the same sightline yet separated in velocity around a galaxy. 25/31 of these are oriented such that the higher EW absorber has the smaller Δv , and the 6 others are close in either velocity or EW . The one galaxy with 3 associated absorbers, NGC1097, shows this trend across two sightlines as well, with absorbers at $\Delta v = 32$ km/s and $EW = 570$ mÅ towards 2dFGRS_S393Z082, and $\Delta v = -39$ km/s and $EW = 184$ mÅ and $\Delta v = 50$ km/s and $EW = 83$ mÅ towards HE0241-3043.

3.4. Azimuth

In this section we examine properties of absorbers as a function of their azimuthal angle with respect to their associated galaxy. Azimuth is defined as the angle between the major axis of a galaxy and the vector connecting the absorption feature and the midpoint of the galaxy plane. Figure 8 illustrates this.

The mean azimuth angle for blueshifted absorbers is 41° , and 45° for redshifted absorbers. Figure 9 shows the distribution of azimuth angles for both red and blue-shifted absorbers. Unlike the findings of Kacprzak et al. (2011, 2012), who find a bimodal distribution of Mg II absorbers around galaxies, our distributions of Ly α absorbers are generally consistent with a flat, or random distribution. There is a slight overabundance of absorbers around 0° azimuth in both red and blue-shifted samples, but we cannot assign this observation much significance yet given the small sample size. We additionally find no significant correlation between azimuth angle and EW or Δv .

4. SUMMARY

We have measured 51 Ly α absorption lines in the spectra of 35 COS targets and matched each to a single, large ($D \geq 25$ kpc) galaxy. Table 3 presents a breakdown of our results when separating absorber-galaxy pairs into red and blue-shifted samples. The following summarizes our findings:

- We introduce a likelihood parameter based on Gaussian profiles centered around ρ/R_{vir} and Δv to automate the matching of absorbers with associated galaxies.
- EW anti-correlates most strongly with ρ when normalized by R_{vir} . It follows that EW weakly correlates and anti-correlates with R_{vir} and ρ , respectively.
- The mean and maximal EW of absorbers increases with decreasing Δv . The strongest absorbers are nearly all found within $\Delta v = \pm 100$ km/s of their associated galaxies.
- We find a slight dichotomy in the EW of absorption blue-ward vs red-ward of associated galaxies. Redshifted absorbers are weaker, with $\overline{EW} = 239 \pm 12$ mÅ compared to $\overline{EW} = 317 \pm 18$ mÅ for blueshifted absorbers.
- Ly α absorbers are most associated with inclined

galaxies. 65% of blueshifted and 75% of redshifted absorbers are associated with galaxies with $i \geq 50$ deg, whereas 56% of all galaxies in the survey volume have similarly high inclinations. The distributions of associated vs all galaxy inclinations differ at a greater than 99% significance level according to the Anderson-Darling distribution test.

- We find no strong azimuth preference for absorption - Ly α absorbers appear to be distributed uniformly around galaxies.

Parameter	Blueshifted	Redshifted
# of systems	23	28
Mean EW [mÅ]	317 ± 18	239 ± 12
Median EW [mÅ]	288 ± 15	177 ± 10
Mean R_{vir} [kpc]	210.7	221.3
Mean ρ [kpc]	222.8	221.3
Mean Δv [km s $^{-1}$]	68	-102
Mean Inc. [deg]	56	59
Mean Az. [deg]	41	45

Table 3
Average properties of the associated galaxy sample split into red and blue-shifted bins based on Δv .